CARDIOVASCULAR MORPHOMETRY WITH HIGH-RESOLUTION 3D MAGNETIC RESONANCE: FIRST APPLICATION TO LEFT VENTRICLE DIASTOLIC DYSFUNCTION

Submitted for the Special Issue

"Frontier Biomechanical Challenges in Cardiovascular Physiopathology", Medical Engineering & Physics

Diego Gallo[a‡], Orestis Vardoulis[b‡], Pierre Monney[c], Davide Piccini[d,e], Panagiotis Antiochos[f], Juerg Schwitter[c], Nikolaos Stergiopulos[g], Umberto Morbiducci[a]

[a] *Department of Mechanical and Aerospace Engineering, Politecnico di Torino, Turin, Italy.*

[b] *Bao Research Group, Department of Chemical Engineering, Stanford University, Stanford CA, USA*

[c] *Division of Cardiology and Cardiac MR Center, University Hospital of Lausanne, Lausanne, Switzerland*

[d] *Department of Radiology, University Hospital and University of Lausanne, Lausanne, Switzerland*

[e] *Advanced Clinical Imaging Technology, Siemens Healthcare AG, Lausanne, Switzerland*

[f] *Division of cardiology, Department of internal medicine, University Hospital of Lausanne, Lausanne, Switzerland*

[g] *Laboratory of Hemodynamics and Cardiovascular Technology, Ecole Polytechnique Fédérale de Lausanne, Lausanne, Switzerland.*

[‡] DG and OV equally contributed to this study

Address for correspondence:

Umberto Morbiducci, Ph.D

Department of Mechanical and Aerospace Engineering, Politecnico di Torino

Corso Duca degli Abruzzi, 24 -- 10129 Turin, Italy

Tel.: +39 011 0906882, Fax: +39 011 5646999

E-mail: umberto.morbiducci@polito.it

Abstract

In this study, an image-based morphometry toolset quantifying geometric descriptors of the left ventricle, aorta and their coupling is applied to investigate whether morphological information can differentiate between subjects affected by diastolic dysfunction (patient group) and their age-matched controls (control group). The ventriculo-aortic region of 20 total participants (10 per group) were segmented from high-resolution 3D magnetic resonance images, from the left ventricle to the descending aorta. Each geometry was divided into segments in correspondence of anatomical landmarks. The orientation of each segment was estimated by least-squares fitting of the respective centerline segment to a plane. Curvature and torsion of vessels' centerlines were automatically extracted, and aortic arch was characterized in terms of height and width.

Tilt angle between subsequent best-fit planes in the left ventricle and ascending aorta regions, curvature and cross-sectional area in the descending aorta resulted significantly different between patient and control groups (*P*-values<0.05). Aortic volume (*P*=0.04) and aortic arch width (*P*=0.03) resulted significantly different between the two groups. The observed morphometric differences underlie differences in hemodynamics, by virtue of the influence of geometry on blood flow patterns.

The present exploratory analysis does not determine if aortic geometric changes precede diastolic dysfunction, or vice versa. However, this study (1) underlines differences between healthy and diastolic dysfunction subjects, and (2) provides geometric parameters that might help to determine early aortic geometric alterations and potentially prevent evolution toward advanced diastolic dysfunction.

Keywords: Thoracic Aorta, Vascular geometry, Geometric risk, Curvature, Torsion

Introduction

Morphometry, i.e., the analysis of a form or shape with quantitative means, has been applied extensively to explore cardiac and vascular anatomy and function. Examples include the detection of anatomical abnormalities [1], preoperative planning and follow-up of patients with cardiovascular diseases [2-4], risk prediction associated to atherosclerosis development [5-8], and cardiovascular devices design support [9]. In particular, morphometry-based analysis finds massive adoption for current research of mapping the effects of natural aging on the structural and functional properties of the aorta [10-17].

Data from those imaging techniques currently adopted in the clinical practice to monitor and assess the cardiovascular function can be leveraged for accurate morphometric analysis. This opens to the possibility of complementing and enriching the information extracted from clinical diagnostic exams. In this regard cardiac magnetic resonance (CMR), bearing the ability to collect precise, quantitative anatomical information, has become a gold standard for heart chambers volumetric analysis and cardiac mass measurements [18, 19]. For these reasons, CMR is widely adopted as diagnostic tool for the assessment of the function of the left ventricle (LV), heart failure (HF), and related pathologies, including diastolic dysfunction [20]. Diastolic dysfunction refers to the pathological condition for which the mechanical function of LV during diastole is abnormal [21]. The hallmarks of LV diastolic dysfunction are impaired relaxation, loss of restoring forces, reduced diastolic compliance, and elevated LV filling pressure [22].

While systolic function can be routinely assessed non-invasively by measuring markers such as LV longitudinal strain, no consensus currently exists on diastolic dysfunction diagnosis, because no effective image-based clinical indicators of diastolic dysfunction have yet been identified (a detailed overview of the strengths and weaknesses of different imaging modalities for evaluating diastolic dysfunction can be found in Flachskampf et al. [22]). This lack in relevant quantification tools results in a vague understanding of the causes leading to diastolic dysfunction. Moreover, in diastolic dysfunction a set of changes in cardiac mass, orientation and function has the potential to affect the mechanical loading and morphology of the aorta. In parallel, induced alterations in the arterial

reflections and in the aortic geometry may result in unfavorable late systolic pressure augmentation, a factor that promotes diastolic dysfunction [22].

In the present study, a morphometry toolset is presented, quantifying geometric descriptors of LV, thoracic aorta and their coupling from 3D CMR images. The proposed toolset is applied to investigate whether the extracted morphological information can be used to differentiate between subjects affected by LV diastolic dysfunction and their age matched controls. The final objective is to investigate if LV diastolic dysfunction is associated with a distortion of the LV-aortic compartment. The proposed image-based morphometric approach could enrich the tools and consequently the information extracted non-invasively, in the direction of understanding the causes and progression of LV diastolic dysfunction [21, 22].

Methods

Image Acquisition

CMR imaging was performed for a population of diseased and healthy subjects with a prototype self-navigated isotropic 3D balanced steady state free-precession (bSSFP) technique that included a radial readout following a spiral phyllotaxis sampling pattern [23]. The technique was adapted for self–navigation [24-26]. The three-dimensional high-resolution CMR image acquisition was performed with a 1.5T clinical MRI scanner (MAGNETOM Aera, Siemens Healthcare GmbH, Erlangen, Germany) and the ECG-triggered acquisition was initiated approximately 4 minutes after injection of a 2mmol/kg bolus of Gadobutrol (Gadovist, Bayer Schering Pharma, Zurich, Switzerland). Imaging parameters included: TR/TE: 3.1/1.56 ms, FOV: 442 mm^3, matrix: 384^3, acquired voxel size: 1.15 mm^3, radio frequency excitation angle 115°, and receiver bandwidth 900 Hz/Pixel. The trigger delay was set to the most quiescent point of mid-diastole.

Study Subjects

The 3D CMR-based morphometric analysis was applied to a dataset of 20 human subjects. Based on CMR acquisitions, subjects were selected to compose two groups: 10 subjects with diastolic dysfunction formed the patient group (PG), while 10 subjects showing normal LV geometry and both systolic/diastolic functions were selected for the control group (CG). Diastolic dysfunction was considered in the presence of (1) normal LV end-diastolic volume, normal LV ejection fraction (>50%) and increased LV mass (>78 g/m^2 in men; >70 g/m^2 in women), (2) increased LV wall thickness (>12 mm), or (3) LV remodeling (mass to LV diastolic volume ratio > 1 g/ml) [21, 22, 27-30].

Patient and control groups were matched for age and gender (in total: 6 females, 14 males; age 58.9±12.5 years, range 39-85 years, body surface area (BSA) 2.0±0.26 m^2, range 1.48-2.53 m^2). The ethics review board approved the experimental protocol, and all of the subjects gave informed consent.

Image segmentation

The cardiovascular regions of interest (ROI) were segmented from the acquired CMR images with a semi-automated expanding region method, that uses a gradient-based edge detection process as implemented in the ITK-SNAP (www.itksnap.org) software [31]. The segmentation process was initiated with a set of manually placed segmentation-defining spheres within the ROI and the corresponding algorithm expands the initial boundaries based on the image data. The cardiovascular structure of the entire aortic trunk including the left ventricle down to the descending thoracic aorta was reconstructed. The descending thoracic aorta was considered to conclude in the level of the renal arteries. The automated segmentation results were visually inspected and any artifacts were corrected with the manual segmentation tool provided by the software. Finally, the segmentation information was exported to stereolithography (STL) file-format for morphometric analysis of the segmented structures.

Morphometric Characterization

The proposed morphometric analysis based the geometric characterization of the anatomical features on the definition of a geometric centerline. In more detail, the centerline **C** is defined and calculated as the locus of the centers of the maximal inscribed spheres along the cardiovascular region of interest. The centerlines are estimated automatically in a form of discrete 3D point sets using the Vascular Modeling Toolkit software (VMTK, www.vmtk.org) [32]. The calculation of local and global features for morphometry characterization is affected by the noise in the estimation of the 3D centerline curves. 3D free-knots regression splines can be employed as a basis of representation to provide a less noisy, analytical formulation of the centerlines [33, 34]. A 3D free-knots regression spline of order *m* is a piecewise polynomial of degree *m-1*, with continuous derivatives of order *m-2* at the spline knots. The number and the position of the knots are not fixed in advance, but chosen to minimize a penalized sum of squared error criterion [35]. In this study, *m* was set equal to six, thus allowing the estimation of an analytical formulation for centerlines with no discontinuities in the derivatives of order up to four.

To simplify the comparisons between subjects, we subdivided the aortic trunk in eight regions (R1 to R8) as defined by nine anatomical landmarks (L1 to L9) positioned in: (1) ventricle apex, (2) ventricle base, (3) aortic valve, (4) pulmonary ascending aorta, (5) brachiocephalic trunk, (6) left subclavian artery, (7) pulmonary descending aorta, (8) diaphragm, and (9) renal level (Figure 1A). In this way, it was possible to break the morphometry analysis in geometric segments. For each centerline segment, a plane fitting the centerline segment was calculated with a least square minimization method, and denoted as best-fit plane in the followings. To characterize the segment orientation, we considered for each plane the normal and tangent vectors, with the latter vector obtained from the linear least-square fit of the projection of the centerline segment onto its respective plane (Figure 1B). The relative orientation of two subsequent best-fit planes was expressed by a tilt (α) and a twist (ϑ) angle, calculated as the arccosine of the internal product between the two tangent vectors and the two normal vectors, respectively [36]. Moreover, twist angle can be related to Euler's rotation theorem, stating that a rotation in the 3D space can be expressed as a single rotation around an axis, which is invariant to the

rotation. The rotation axis is determined as the line of intersection between the two planes, and the rotation around it is quantified by the twist angle (also called dihedral angle).

By differentiation of the free-knots regression spline, the centerlines are characterized on the basis of curvature and torsion. The curvature κ and the torsion τ of a curve **C** along the curvilinear abscissa s are defined as:

$$\kappa(s) = \frac{\left|\mathbf{C}'(s) \times \mathbf{C}''(s)\right|}{\left|\mathbf{C}'(s)\right|^3} \qquad (1)$$

$$\tau(s) = \frac{\left[\mathbf{C}'(s) \times \mathbf{C}''(s)\right] \cdot \mathbf{C}'''(s)}{\left|\mathbf{C}'(s) \times \mathbf{C}''(s)\right|^2} \qquad (2)$$

where primes denote derivatives of the curve **C** with respect to the curvilinear abscissa s. Curvature is defined as the reciprocal of the radius of the circle lying on the plane defined by the normal and tangent vector to the curve at that point (osculating plane, Figure 2) and it measures the rate of change in the tangent vector orientation along the curve. Torsion measures the deviation of the curve from the osculating plane (Figure 2). Both parameters are known to have a major influence on hemodynamics [37, 38]. Cross-sectional area A(s) was also considered for geometric characterization. Cross-sectional areas were calculated automatically via intersection of a plane normal to the centerline at the desired location.

Quantitative geometric measures were derived from the characterization described in the previous section.

For each segment (corresponding to regions R1 to R8), the maximum, average and peak-to-peak amplitude (i.e., max-min) values (indicated as Max, Avg and PP) were estimated for curvature, torsion and cross-sectional area. The minimum cross-sectional area (Min A) for each segment was considered, as abrupt transitions to lower values may denote the existence of a constriction. The tilt and twist angles between planes fitting consecutive centerline segments were evaluated as a measure of orientation change along the centerline.

A set of global parameters was also considered. The BSA-adjusted values of total aortic volume were estimated. Aortic arch width (W) was defined as the distance between the centerline points of the ascending and descending

aorta at the level of the pulmonary artery [39]. The height H of the aortic arch was defined as the distance between W and the highest centerline point of the aortic arch in left anterior oblique projection [39]. The ratio H/W was also quantified. Left ventricle shape was evaluated as based on the sphericity index (SI), which is defined as the ratio between the ventricle long axis (measured from the apex to the mid-point of the mitral valve) over the short axis (equivalent diameter of the ventricle section that perpendicularly intersects the long axis mid-point).

To test for differences between the groups (CG *vs*. PG), the univariate Mann-Whitney non-parametric U test was applied, for all the vascular segments and descriptors. Significant level was set at $P < 0.05$. The calculation of morphometric parameters and the statistical analysis were performed using VMTK libraries and Matlab (The MathWorks, Natick, MA, USA).

Results

The complete set of reconstructed geometries for patient and control groups is presented in Figure 3 (top and bottom row, respectively), along with the corresponding centerlines.

Local curvature and torsion profiles provide a representation of the spatial variations in geometric attributes of ventricle-aorta regions, showing their complex geometric characteristics, non-uniformity and non-planarity (Figure 4). In particular, most subjects present peak values for curvature located close to the aortic valve (R1) or in the proximal descending aorta (R6). Considerable absolute peak values for torsion are shown by some geometries (up to 6 mm^{-1}, M74 subject in the PG, but also, e.g., M67 subject in the PG, and M39 subject in the CG).

Cross sectional areas are reported in Figure 5. As expected, the largest cross-sectional areas are found within the limits of region R1. Moving downstream, the cross-sectional areas show a sudden decrease due to the aortic valve (R2 in Figure 5), followed by an increase in correspondence of the sinuses of Valsalva. A slow decrease (due to the aortic tapering) is then shown along the curvilinear coordinate *s* in the arch and descending aorta regions, as expected (Figure 5).

Results from the quantitative geometric characterization were used for statistical analysis and are summarized in Tables 1 and 2 for regional and global parameters respectively. Statistically significant differences between control and patient groups were observed with the current morphometric analysis. In particular, the tilt angle α was shown to be significantly different in regions R1, R2 and R3, while the twist angle ϑ was shown to be significantly different in region R3. Significant differences between the two groups were also shown for curvature-derived parameters in the descending aorta (R8). In regards to torsion, differences in average torsion were not significant in any of the regions, while torsion maximum values presented significant differences in region R2, and peak-to-peak amplitude values of torsion presented significant differences in regions R1, R2 and R3. Descriptors derived from cross-sectional areas yielded significant differences in one region or more (Avg A: R7; Max A: R4; Min A: R1, R7; PP A: R3, R4, data presented in Table 1). Considering global geometric parameters, the statistical analysis is reported in Table 2. Total aortic volume as well as aortic arch width presented significant difference between the two groups with P=0.038, and P=0.032 respectively. Sphericity index SI, aortic arch height H and the ratio H/W were not significantly different between the two groups.

In order to visually evaluate differences in the distributions of the descriptors yielding statistically significant differences, box plots were generated and are shown in Figure 6, where the median, the interquartile range and the extreme values for a 95% coverage of the distribution are depicted. The boxplots provide clear observation that the median values of the considered descriptors were different for the two groups, as given by the statistical test, and that in most cases also both the spread and symmetry of the distributions of considered data were different.

Discussion

In diastolic dysfunction, LV abnormalities in mass, orientation and mechanical function during diastole affect the mechanical loading and morphology of the aorta. In parallel, alterations in aortic morphology may promote diastolic dysfunction via altered hemodynamics and late systolic pressure augmentation due to altered pressure wave reflections [22]. Thus, open questions still exist on whether diastolic dysfunction is due to a specific cardiac

207 disease or it is the result of a myocardial response to unfavorable working conditions attributable to the
208 downstream arterial system (e.g., arterial stiffening) [22].
209 In this study, we demonstrated the potential of morphometric analysis of the ventriculo-aortic region for
210 investigating differences between healthy and diastolic dysfunction subjects. Technically, 3D models of the
211 ventriculo-aortic structure were reconstructed from 3D CMR images, and morphometric analysis was performed
212 by considering global and regional parameters, as defined by anatomical landmarks.
213 The regional analysis identified statistically significant differences between CG and PG (1) in the LV and ascending
214 aorta regions (R1:R3), specifically in the tilt angle α and the dynamic range of torsion (Table 1), and (2) in the
215 distal descending aorta (R7, R8), where differences in parameters derived from curvature and area emerged.
216 Considering global variables, significant differences between CG and PG were observed in the aortic volume and
217 aortic arch width (Table 2). Interestingly, the PG exhibited considerably less geometric variability than CG when
218 considering torsion-based parameters (Figure 6), suggesting relative homogeneity of those parameters in PG
219 subjects.
220 The observed morphometric differences imply differences in hemodynamics, by virtue of the influence of
221 geometry on blood flow patterns [5-7, 40]. In particular, the tilt and twist angles quantify the “distortion” of the
222 aorta, which is expected to impart an abrupt change in the direction of blood flow. Here, it was found that aortic
223 distortion is more pronounced in the PG, therefore the underlying flow patterns are expected to be more intricate
224 and complex for the PG [41] than for the CG. The distortion observed in PG, and the consequent reshaping
225 imposed to flow structures, does represent a point of attention, because curvature and torsion have a well-known
226 influence on arterial hemodynamics, in particular on the arrangement of flow in helical structures, that has been
227 reported to limit flow disturbances [42-44].
228 Aortic cross-sectional area has also been considered as it influences flow rate, Reynolds number, arterial
229 resistance and the presence of helical flow [41]. Area-based parameters and aortic volume allow to quantitatively
230 describe aortic enlargement, that has been correlated with arterial stiffening [45] and, ultimately, to systemic risk
231 factors such as hypertension. Among possible scenarios, an increased aortic volume, as the one observed here for

PG (Figure 6), might progressively lead over time to chronically increased LV afterload, promoting LV hypertrophy and concentric remodeling [46], consistently with the diastolic dysfunction diagnosis of PG.

Furthermore, the ascending aorta is a major contributor to the systemic total compliance of the arterial tree, and several previous reports demonstrate the existence of a complex interplay between aortic pulse wave velocity (PVW) and LV remodeling. In particular, Redheuil et al. [16] demonstrated the existence of a significant relationship between increased arch width, increased PWV, decreased aortic arch distensibility and increased LV mass and concentric remodeling, in accordance with the results of the present study (aortic arch width resulted statistically different between CG and PG, with higher values for PG, Table 2 and Figure 6). In addition, a large H/W ratio has been identified as possible promoter of increased pulse pressure and PWV, enhanced systolic wave reflection and increased wall shear stress, likely inducing structural changes in the aortic wall [47]. Notwithstanding these factors are well-known contributors to LV remodeling [16, 48], in this study no statistically significant difference between CG and PG was observed, when evaluating the H/W ratio. Moreover, although sphericity has been indicated as a marker of cardiomyopathy [30], differences between PG and CG were not found.

It is worth noting that the cross-sectional design of the present study does not allow to answer the question whether geometric changes precede diastolic dysfunction, or vice versa. A highly complex and dynamic interplay exists among the processes leading to diastolic dysfunction, aortic morphology, and the underlying hemodynamics. As the pathology progresses, the relationship evolves determining a disease-driven remodeling of the aortic geometry. In this context, it is accepted that the aorta remodels its geometry, structure and composition according to an overall optimization strategy. Among the factors regulating the remodeling, we mention here the magnitude of the circumferential stress in the arterial wall, the flow-induced shear stress at the inner surface, that needs to be maintained within the physiological range [49], and the remodeling action of altered pressure levels, which are commonly found in diastolic dysfunction patients [21, 50]. Notwithstanding the intricacy of the relationship geometry - diastolic dysfunction, questions cannot be answered without knowledge of the several risk factors, and thus we focus in this preliminary study on the geometric differences between PG

and CG. As further limitation, no data on blood pressure levels or other parameters such as blood flow data or vessel distensibility were recorded. The focus on geometric factors is motivated by the easiness of their acquisition in the clinical practice, although this limits the comparability of our results with findings in similar patient cohorts. A further shortcoming is the limited number of subjects included in the study.

The limitations listed above make the analysis here presented to be intended as exploratory, whose main aims are the setting up of an image-based tool, and the identification of candidate morphometric descriptors for a next, adequately powered study. In particular, this work represents the first systematic and statistical analysis on diastolic dysfunction considering, among others, factors such as tilt/twist angles, and local curvature and torsion, indicators of the presence of distortive cardiovascular mechanisms. Quantitative geometric characterization by the robust and noninvasive methods described in this work can be easily and robustly obtained from imaging data and employed at a large scale for explorative studies, clinical trials and ultimately clinical routine. Moreover, the proposed approach might provide proofs-of-concept for further in vivo investigations to determine valuable new markers of diastolic dysfunction-related alterations, allowing an early diagnosis of the LV remodeling and dysfunction. The developed methods could also be extended to assess a whole range of other situations, such as the investigation of vascular remodeling after successful repair of aortic coarctation. As further development, the proposed morphometric analysis could be integrated with a in vivo quantitative hemodynamics based on 4D flow MRI. Such technique would allow to estimate hemodynamic quantities like pulse wave velocity [51, 52], and helical flow [17, 43].

In conclusion, we developed a platform to perform morphometric analysis of the ventriculo-aortic region to identify differences between healthy and diastolic dysfunction subjects, and to understand the clinical implications of altered geometries. The morphometric parameters defined in this study could help to determine early aortic geometric alterations and potentially prevent evolution toward advanced LV remodeling and diastolic dysfunction. Further initiatives should focus on processing larger databases in order to evaluate any diagnostic or risk stratification value of the parameters.

Acknowledgments

OV acknowledges the Swiss National Science Foundation for his Early Postdoc Mobility research fellowship.

References

[1] Kleinert S, Geva T. Echocardiographic Morphometry and Geometry of the Left-Ventricular Outflow Tract in Fixed Subaortic Stenosis. J Am Coll Cardiol. 1993;22:1501-8.

[2] Schumacher H, Eckstein HH, Kallinowski F, Allenberg JR. Morphometry and classification in abdominal aortic aneurysms: Patient selection for endovascular and open surgery. J Endovasc Surg. 1997;4:39-44.

[3] Nakatamari H, Ueda T, Ishioka F, Raman B, Kurihara K, Rubin GD, et al. Discriminant analysis of native thoracic aortic curvature: risk prediction for endoleak formation after thoracic endovascular aortic repair. Journal of vascular and interventional radiology : JVIR. 2011;22:974-9 e2.

[4] Hasegawa T, Oshima Y, Maruo A, Matsuhisa H, Tanaka A, Noda R, et al. Aortic arch geometry after the Norwood procedure: The value of arch angle augmentation. The Journal of thoracic and cardiovascular surgery. 2015;150:358-66.

[5] Friedman MH, Deters OJ, Mark FF, Bargeron CB, Hutchins GM. Arterial geometry affects hemodynamics. A potential risk factor for athersoclerosis. Atherosclerosis. 1983;46:225-31.

[6] Lee SW, Antiga L, Spence JD, Steinman DA. Geometry of the carotid bifurcation predicts its exposure to disturbed flow. Stroke. 2008;39:2341-7.

[7] Bijari PB, Antiga L, Gallo D, Wasserman BA, Steinman DA. Improved prediction of disturbed flow via hemodynamically-inspired geometric variables. J Biomech. 2012;45:1632-7.

[8] Morbiducci U, Kok AM, Kwak BR, Stone PH, Steinman DA, Wentzel JJ. Atherosclerosis at arterial bifurcations: evidence for the role of haemodynamics and geometry. Thrombosis and haemostasis. 2016;115:484-92.

[9] Ellwein L, Marks DS, Migrino RQ, Foley WD, Sherman S, LaDisa JF, Jr. Image-based quantification of 3D morphology for bifurcations in the left coronary artery: Application to stent design. Catheterization and cardiovascular interventions : official journal of the Society for Cardiac Angiography & Interventions. 2016;87:1244-55.

[10] Mao SS, Ahmadi N, Shah B, Beckmann D, Chen A, Ngo L, et al. Normal thoracic aorta diameter on cardiac computed tomography in healthy asymptomatic adults: impact of age and gender. Academic radiology. 2008;15:827-34.

[11] Wolak A, Gransar H, Thomson LE, Friedman JD, Hachamovitch R, Gutstein A, et al. Aortic size assessment by noncontrast cardiac computed tomography: normal limits by age, gender, and body surface area. JACC Cardiovascular imaging. 2008;1:200-9.

[12] Sugawara J, Hayashi K, Yokoi T, Tanaka H. Age-associated elongation of the ascending aorta in adults. JACC Cardiovasc Imaging. 2008;1:739-48.

[13] Lin FY, Devereux RB, Roman MJ, Meng J, Jow VM, Jacobs A, et al. Assessment of the thoracic aorta by multidetector computed tomography: age- and sex-specific reference values in adults without evident cardiovascular disease. Journal of cardiovascular computed tomography. 2008;2:298-308.

[14] Lin FY, Devereux RB, Roman MJ, Meng J, Jow VM, Simprini L, et al. The right sided great vessels by cardiac multidetector computed tomography: normative reference values among healthy adults free of cardiopulmonary disease, hypertension, and obesity. Academic radiology. 2009;16:981-7.

[15] Craiem D, Chironi G, Redheuil A, Casciaro M, Mousseaux E, Simon A, et al. Aging impact on thoracic aorta 3D morphometry in intermediate-risk subjects: looking beyond coronary arteries with non-contrast cardiac CT. Ann Biomed Eng. 2012;40:1028-38.

[16] Redheuil A, Yu WC, Mousseaux E, Harouni AA, Kachenoura N, Wu CO, et al. Age-related changes in aortic arch geometry: relationship with proximal aortic function and left ventricular mass and remodeling. J Am Coll Cardiol. 2011;58:1262-70.

[17] Garcia J, Barker AJ, Murphy I, Jarvis K, Schnell S, Collins JD, et al. Four-dimensional flow magnetic resonance imaging-based characterization of aortic morphometry and haemodynamics: impact of age, aortic diameter, and valve morphology. European heart journal cardiovascular Imaging. 2016;17:877-84.

[18] Rademakers FE. Magnetic resonance imaging in cardiology. Lancet. 2003;361:359-60.

[19] Hauser TH, McClennen S, Katsimaglis G, Josephson ME, Manning WJ, Yeon SB. Assessment of left atrial volume by contrast enhanced magnetic resonance angiography. Journal of cardiovascular magnetic resonance : official journal of the Society for Cardiovascular Magnetic Resonance. 2004;6:491-7.
[20] Redfield MM. Understanding "diastolic" heart failure. The New England journal of medicine. 2004;350:1930-1.
[21] Zile MR, Brutsaert DL. New concepts in diastolic dysfunction and diastolic heart failure: Part I: diagnosis, prognosis, and measurements of diastolic function. Circulation. 2002;105:1387-93.
[22] Flachskampf FA, Biering-Sorensen T, Solomon SD, Duvernoy O, Bjerner T, Smiseth OA. Cardiac Imaging to Evaluate Left Ventricular Diastolic Function. JACC Cardiovascular imaging. 2015;8:1071-93.
[23] Piccini D, Littmann A, Nielles-Vallespin S, Zenge MO. Spiral phyllotaxis: the natural way to construct a 3D radial trajectory in MRI. Magnetic resonance in medicine. 2011;66:1049-56.
[24] Piccini D, Littmann A, Nielles-Vallespin S, Zenge MO. Respiratory self-navigation for whole-heart bright-blood coronary MRI: methods for robust isolation and automatic segmentation of the blood pool. Magnetic resonance in medicine. 2012;68:571-9.
[25] Piccini D, Monney P, Sierro C, Coppo S, Bonanno G, van Heeswijk RB, et al. Respiratory self-navigated postcontrast whole-heart coronary MR angiography: initial experience in patients. Radiology. 2014;270:378-86.
[26] Monney P, Piccini D, Rutz T, Vincenti G, Coppo S, Koestner SC, et al. Single centre experience of the application of self navigated 3D whole heart cardiovascular magnetic resonance for the assessment of cardiac anatomy in congenital heart disease. Journal of cardiovascular magnetic resonance : official journal of the Society for Cardiovascular Magnetic Resonance. 2015;17:55.
[27] Paulus WJ, Tschope C, Sanderson JE, Rusconi C, Flachskampf FA, Rademakers FE, et al. How to diagnose diastolic heart failure: a consensus statement on the diagnosis of heart failure with normal left ventricular ejection fraction by the Heart Failure and Echocardiography Associations of the European Society of Cardiology. European heart journal. 2007;28:2539-50.
[28] Yturralde RF, Gaasch WH. Diagnostic criteria for diastolic heart failure. Progress in cardiovascular diseases. 2005;47:314-9.
[29] Zile MR, Gaasch WH, Carroll JD, Feldman MD, Aurigemma GP, Schaer GL, et al. Heart failure with a normal ejection fraction: is measurement of diastolic function necessary to make the diagnosis of diastolic heart failure? Circulation. 2001;104:779-82.
[30] Adhyapak SM, Menon PG, Parachuri VR. Characterization of Left Ventricular Regional Morphology and Function Using Cardiac Magnetic Resonance for Planning Optimal Surgical Ventricular Restoration. Circulation. 2013;128.
[31] Yushkevich PA, Piven J, Hazlett HC, Smith RG, Ho S, Gee JC, et al. User-guided 3D active contour segmentation of anatomical structures: significantly improved efficiency and reliability. NeuroImage. 2006;31:1116-28.
[32] Antiga L, Piccinelli M, Botti L, Ene-Iordache B, Remuzzi A, Steinman DA. An image-based modeling framework for patient-specific computational hemodynamics. Medical & biological engineering & computing. 2008;46:1097-112.
[33] Sangalli LM, Secchi P, Vantini S, Veneziani A. Efficient estimation of three-dimensional curves and their derivatives by free-knot regression splines, applied to the analysis of inner carotid artery centrelines. Journal of the Royal Statistical Society Series C-Applied Statistics. 2009;58:285-306.
[34] Morbiducci U, Gallo D, Cristofanelli S, Ponzini R, Deriu MA, Rizzo G, et al. A rational approach to defining principal axes of multidirectional wall shear stress in realistic vascular geometries, with application to the study of the influence of helical flow on wall shear stress directionality in aorta. J Biomech. 2015;48:899-906.
[35] Zhou SG, Shen XT. Spatially adaptive regression splines and accurate knot selection schemes. Journal of the American Statistical Association. 2001;96:247-59.
[36] Manbachi A, Hoi Y, Wasserman BA, Lakatta EG, Steinman DA. On the shape of the common carotid artery with implications for blood velocity profiles. Physiological measurement. 2011;32:1885-97.
[37] Germano M. On the Effect of Torsion on a Helical Pipe-Flow. Journal of Fluid Mechanics. 1982;125:1-8.

[38] Alastruey J, Siggers JH, Peiffer V, Doorly DJ, Sherwin SJ. Reducing the data: Analysis of the role of vascular geometry on blood flow patterns in curved vessels. Physics of Fluids. 2012;24.
[39] Ou P, Bonnet D, Auriacombe L, Pedroni E, Balleux F, Sidi D, et al. Late systemic hypertension and aortic arch geometry after successful repair of coarctation of the aorta. European Heart Journal. 2004;25:1853-9.
[40] Gallo D, Steinman DA, Morbiducci U. An insight into the mechanistic role of the common carotid artery on the hemodynamics at the carotid bifurcation. Annals of biomedical engineering. 2015;43:68-81.
[41] Frydrychowicz A, Berger A, Munoz Del Rio A, Russe MF, Bock J, Harloff A, et al. Interdependencies of aortic arch secondary flow patterns, geometry, and age analysed by 4-dimensional phase contrast magnetic resonance imaging at 3 Tesla. European radiology. 2012;22:1122-30.
[42] Morbiducci U, Ponzini R, Gallo D, Bignardi C, Rizzo G. Inflow boundary conditions for image-based computational hemodynamics: impact of idealized versus measured velocity profiles in the human aorta. J Biomech. 2013;46:102-9.
[43] Morbiducci U, Ponzini R, Rizzo G, Cadioli M, Esposito A, Montevecchi FM, et al. Mechanistic insight into the physiological relevance of helical blood flow in the human aorta: an in vivo study. Biomechanics and modeling in mechanobiology. 2011;10:339-55.
[44] Liu X, Sun A, Fan Y, Deng X. Physiological significance of helical flow in the arterial system and its potential clinical applications. Annals of biomedical engineering. 2015;43:3-15.
[45] Hickson SS, Butlin M, Graves M, Taviani V, Avolio AP, McEniery CM, et al. The relationship of age with regional aortic stiffness and diameter. JACC Cardiovascular imaging. 2010;3:1247-55.
[46] O'Rourke M. Arterial stiffening and vascular/ventricular interaction. Journal of human hypertension. 1994;8 Suppl 1:S9-15.
[47] Ou P, Celermajer DS, Raisky O, Jolivet O, Buyens F, Herment A, et al. Angular (Gothic) aortic arch leads to enhanced systolic wave reflection, central aortic stiffness, and increased left ventricular mass late after aortic coarctation repair: evaluation with magnetic resonance flow mapping. The Journal of thoracic and cardiovascular surgery. 2008;135:62-8.
[48] Toprak A, Reddy J, Chen W, Srinivasan S, Berenson G. Relation of pulse pressure and arterial stiffness to concentric left ventricular hypertrophy in young men (from the Bogalusa Heart Study). The American journal of cardiology. 2009;103:978-84.
[49] Glagov S. Intimal hyperplasia, vascular modeling, and the restenosis problem. Circulation. 1994;89:2888-91.
[50] Schillaci G, Pasqualini L, Verdecchia P, Vaudo G, Marchesi S, Porcellati C, et al. Prognostic significance of left ventricular diastolic dysfunction in essential hypertension. J Am Coll Cardiol. 2002;39:2005-11.
[51] Wentland AL, Wieben O, Francois CJ, Boncyk C, Del Rio AM, Johnson KM, et al. Aortic pulse wave velocity measurements with undersampled 4D flow-sensitive MRI: comparison with 2D and algorithm determination. Journal of Magnetic Resonance Imaging. 2013;37:853-9.
[52] Dyverfeldt P, Ebbers T, Lanne T. Pulse wave velocity with 4D flow MRI: Systematic differences and age-related regional vascular stiffness. Magnetic Resonance Imaging. 2014;32:1266-71.

Tables

Table 1. Tabularized version of *P* values for all regional parameters (bold values stand for $P<0.05$). κ, τ and A correspond to curvature, torsion and cross sectional area, while Max, Avg, PP and Min correspond to maximum, average, peak-to-peak amplitude and minimum values.

***P* values**	R1	R2	R3	R4	R5	R6	R7	R8
Tilt angle α	**0.019**	**0.027**	**0.013**	0.396	0.312	0.172	0.353	0.298
Twist angle ϑ	0.425	0.121	**0.038**	0.455	0.425	0.440	0.367	0.339
Avg κ	0.367	0.061	0.192	0.061	0.093	0.172	0.312	0.137
Max κ	0.260	0.367	0.425	0.367	0.214	0.485	0.260	**0.027**
PP κ	0.260	0.339	0.214	0.367	0.485	0.339	0.367	**0.044**
Avg τ	0.260	0.312	0.285	0.172	0.455	0.260	0.367	0.192
Max τ	0.061	**0.027**	0.093	0.425	0.515	0.396	0.214	0.192
PP τ	**0.038**	**0.011**	**0.019**	0.339	0.485	0.425	0.214	0.106
Avg A	0.106	0.236	0.106	0.061	0.192	0.154	**0.038**	0.061
Max A	0.455	0.425	0.081	**0.027**	0.192	0.236	0.061	0.052
Min A	**0.032**	0.154	0.061	0.172	0.214	0.154	**0.038**	0.075
PP A	0.214	0.285	**0.023**	**0.044**	0.285	0.396	0.367	0.172

Table 2. Tabularized version of *P* values for global parameters (bold values stand for *P*<0.05). *V, H* and *W* correspond to volume, arch height and arch width, respectively.

	***P* values**
Volume V	**0.038**
Arch Width W	**0.032**
Arch Height H	0.285
H/W	0.214

Figures captions

Figure1 - (A) Representation of the human aorta with the landmarks L1-L9 defining the arterial segments (R1-R8) on which the regional morphometric analysis was performed; (B) example of geometry showing the centerline and two best-fit planes. From each best-fit plane, the normal vector (red color) and the tangent vector (blue color) are shown. The angle between two consecutive normal vectors is the twist angle (ϑ), while the angle between two consecutive tangent vectors is the tilt angle (α).

Figure 2 - Curvature and torsion definition. Curve a has curvature κ and torsion τ equal to zero. Curve b lies in a plane and has non-zero curvature (equal to 1/R in the point tangent to the shown circle), but zero torsion. Curve c leaves the plane, and has non-zero curvature and non-zero torsion.

Figure 3 - 3D visualization of the aortic geometries for patient group PG and control group CG. M stands for male, F for female and the number indicates the age. Centerlines are colored by curvature values.

Figure 4 - Longitudinal profiles of curvature (κ) and torsion (τ) as generated for all geometries by using 3D free-knots regression splines representation. The varying severity of curvature and torsion along curvilinear coordinate *s* highlights the complex geometry and non-planarity.

Figure 5 - Longitudinal profiles of cross-sectional area (A) as generated for all geometries by using 3D free-knots regression splines representation.

Figure 6 - Boxplots for the descriptors yielded as statistically significantly different. The median is indicated by the red line, the blue box indicates the interquartile range and the whiskers indicate the extreme values for a 95% coverage of the distribution.

Figures

Figure 1.

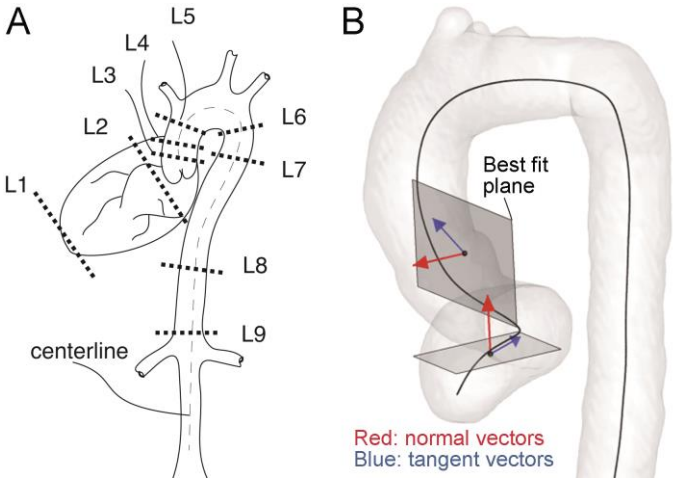

455 Figure 2

456

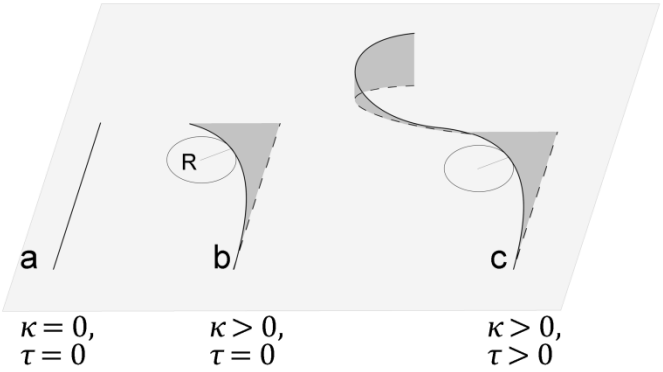

457

458 Figure 3

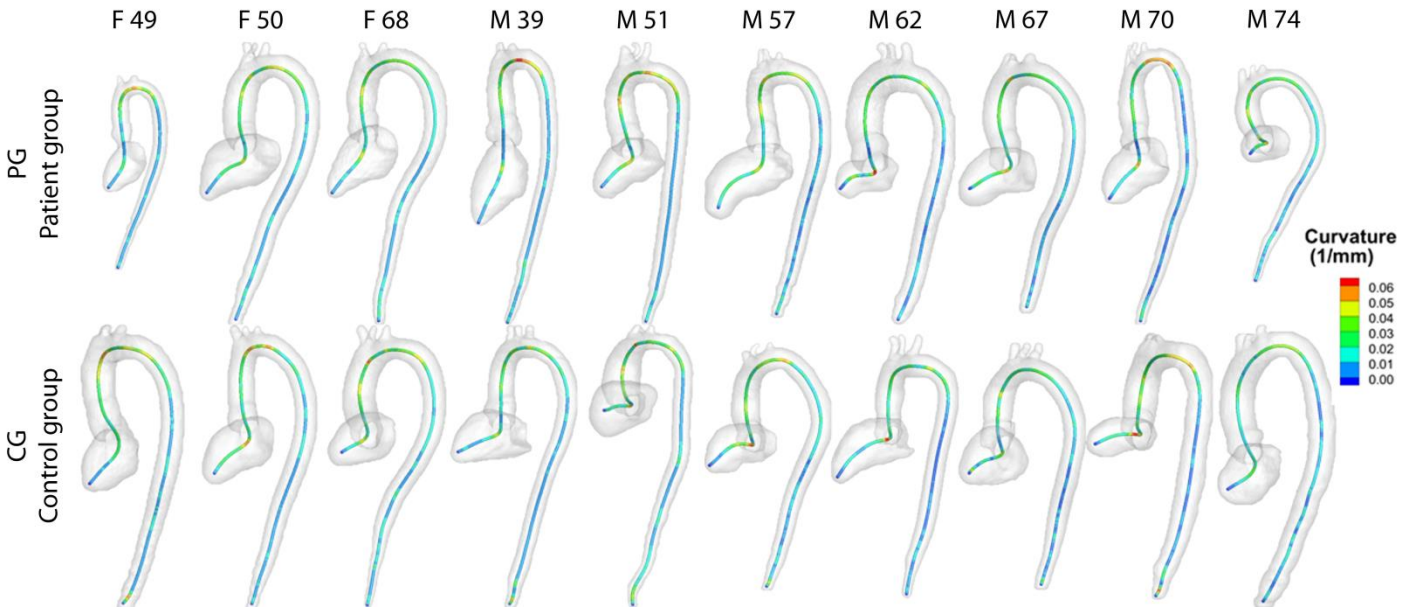

459

460 Figure 4

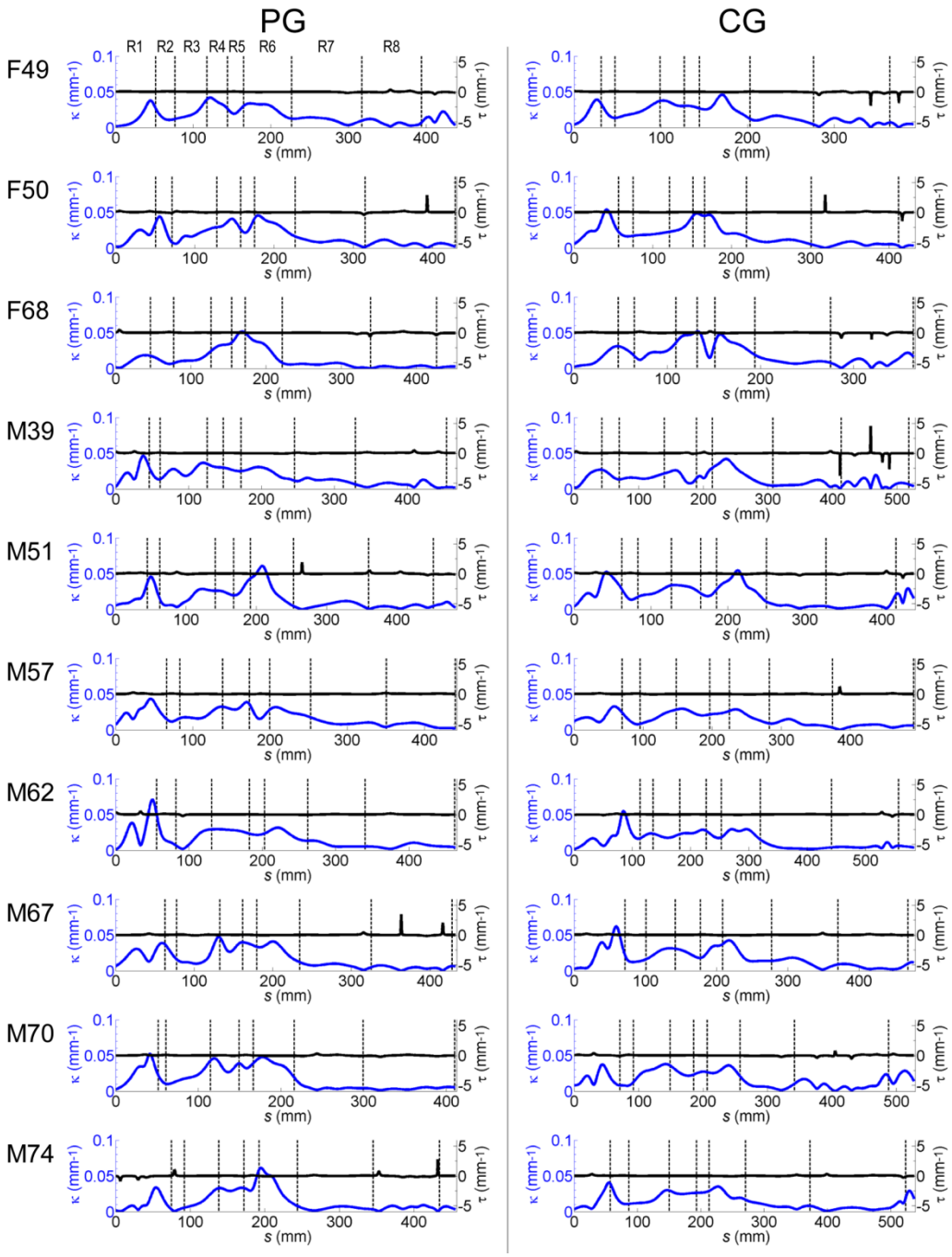

461

462 Figure 5.

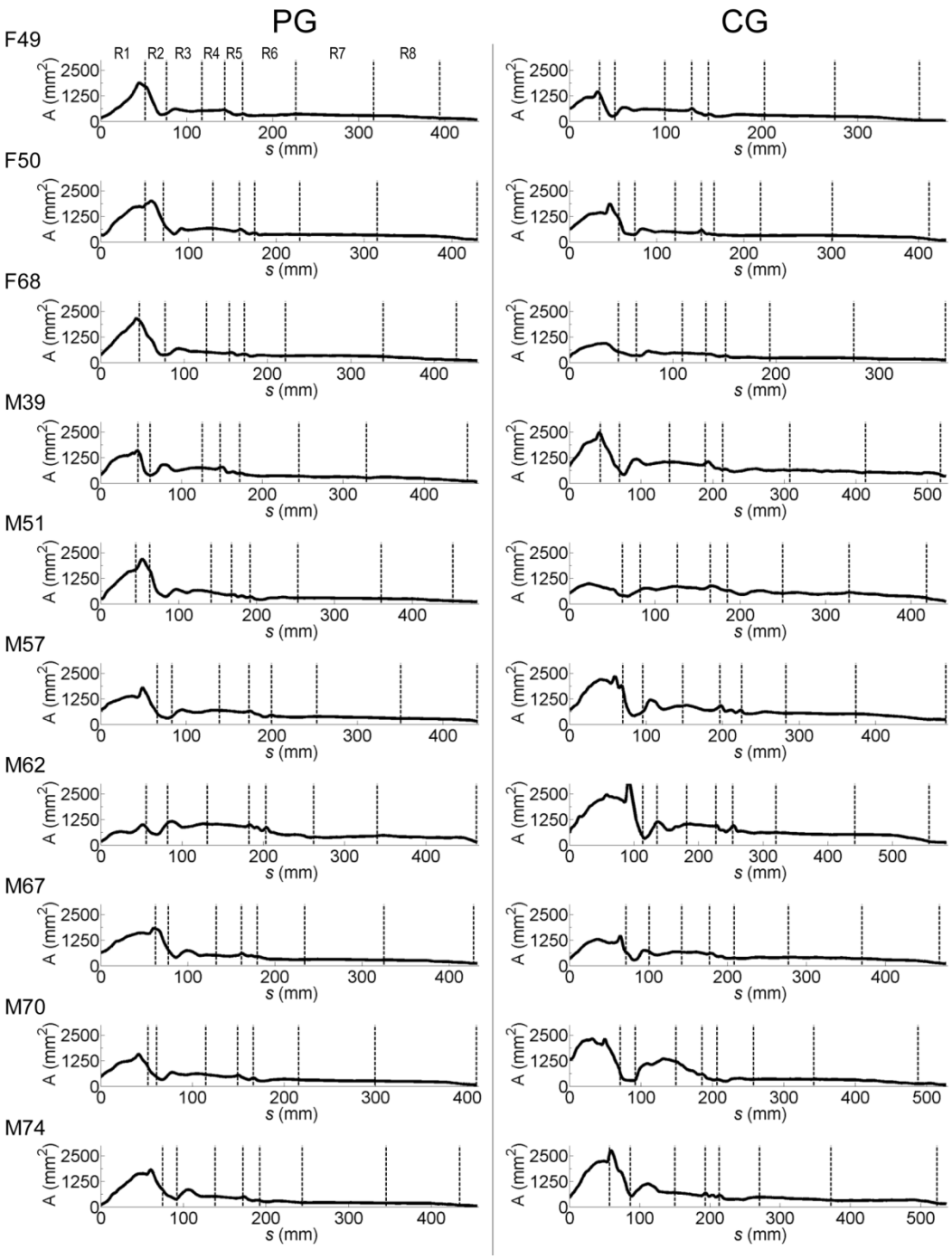

463

464 Figure 6.

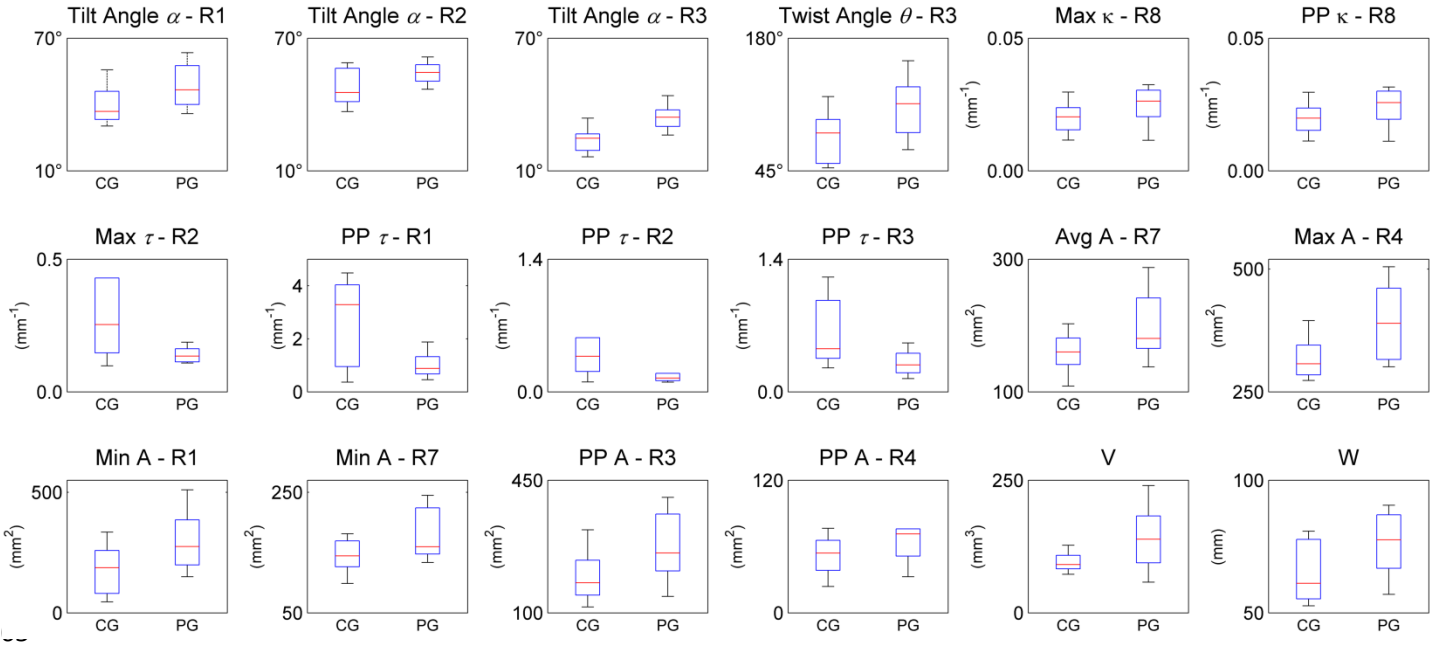

466